Characteristics of precipitating energetic electron fluxes relative to the plasmapause during geomagnetic storms

Ian C. Whittaker,[1] Mark A. Clilverd,[2] Craig J. Rodger[1]

Corresponding author: I. Whittaker, Department of Physics, University of Otago, PO Box 56, Dunedin 9054, New Zealand. (ian.whittaker@otago.ac.nz)

[1]Department of Physics, University of Otago, Dunedin, New Zealand.

[2]British Antarctic Survey (NERC), Cambridge, UK.

Abstract. In this study we investigate the link between precipitating electrons from the Van Allen radiation belts and the dynamical plasmapause. We consider electron precipitation observations from the POES satellite constellation during geomagnetic storms. Superposed epoch analysis is performed on precipitating electron observations for the 13 year period of 1999 to 2012 in two MLT sectors, morning and afternoon. We assume the precipitation is due to wave particle interactions and our two MLT sectors focus on chorus (outside the plasmapause) and plasmapspheric hiss (inside the plasmapause) waves. We generate simple expressions based on the geomagnetic index, Dst, which reproduce the chorus-driven observations for the >30 keV precipitating electron flux magnitudes. Additionally, we find expressions for the fitted spectral index to describe the flux variation with energy, allowing a full energy reproduction as a function of distance from the plasmapause. The hiss-driven precipitating flux occurs inside the plasmapause, but is independent of distance from the plasmapause. In the POES observations the hiss induced electron precipitation is only detectable above the instrument noise in the >300 keV and P6 (>800 keV) channels of the flux detection instrument. We have derived expressions for the storm-time variation in flux inside the plasmapause using Dst as a proxy. The observations show there is little evidence for >800 keV electron precipitation occurring outside of the plasmapause, in the MLT sectors studied.

1. Introduction

Energetic electron precipitation (EEP), which is strongest during geomagnetic storms, is of great interest to radiation belt and atmospheric scientists. The particle energy determines the altitude in the atmosphere at which the majority of its energy is deposited [e.g., *Turunen et al.*, 2009, Fig.3]. Electrons with energies ∼100 keV cause peak ionization changes at ∼80 km altitude while ∼1 MeV electron energy peaks at ∼62 km altitude. This has major implications for atmospheric chemistry as precipitating charged particles produce odd nitrogen (NO_x [*Newnham et al.*, 2011]) and odd hydrogen (HO_x [*Verronen et al.*, 2011]) in the Earth's atmosphere. These odd particles can then catalytically destroy ozone due to their longer lifetime at these altitudes [*Thorne*, 1977, 1980; *Solomon, Crutzen and Roble*, 1982; *Brasseur and Solomon*, 2005; *Verronen et al.*, 2013] and have been linked to variability in surface climate [*Seppälä et al.*, 2013]. In particular, *Andersson et al.* [2012] reported experimental evidence of electron precipitation producing odd hydrogen changes, during geomagnetic storms, stretching over the altitude range of ∼52 to 82 km, corresponding to electrons from ∼100 keV to ∼3 MeV. These authors recently showed that atmospheric HO_x increases during geomagnetic storms at atmospheric locations under the radiation belts [*Andersson et al.*, 2014].

In the radiation belts wave-particle interactions can cause pitch angle [*Lakhina et al.*, 2010] and energy [*Meredith et al.*, 2002] diffusion. For a recent review on wave-particle interaction, see *Thorne* [2010]. In the VLF range one important type of wave is whistler-mode chorus, while in the ULF range attention tends to focus on EMIC (ElectroMagnetic

Ion Cyclotron) waves [*Horne and Thorne*, 1998]. Chorus is observed in the frequency range of a few hundred Hz to several kHz [*Helliwell*, 1969] and occurs in the morning MLT region outside the plasmapause [*Summers, Thorne and Xiao*, 1998]. There have been many studies which have linked chorus waves to intense energetic electron precipitation [e.g. *Hikishima, Omura and Summers*, 2010; *Lam et al.*, 2010; *Meredith et al.*, 2011], as expected from the strong wave amplitudes. Plasmaspheric hiss occurs in the inner magnetosphere over a band between 100 Hz and 2 kHz [*Summers, et al.*, 2008]. Hiss induced electron precipitation has been shown to be responsible for the formation of the slot region between the inner and outer radiation belts [*Lyons and Thorne*, 1973]. Long-lasting plasmaspheric hiss-driven precipitation has been monitored from the ground [*Rodger et al.*, 2007], and shown to be able to produce significant ozone depletions [*Rodger et al.*, 2010a].

It has long been recognized that there is a link between the dynamical plasmapause location and the trapped fluxes in the outer radiation belt. Observations of relativistic electrons from SAMPEX showed that over time periods of weeks to months the plasmapause location was a good indication of the inner edge of the outer radiation belt [*Li et al.*, 2006]. This correlation demonstrates how differing wave activity inside and outside the plasmapause strongly determines the long term variation in the trapped flux magnitudes and location. The same study, however, demonstrated that this relationship breaks down on shorter time periods. This is clearest for events where the plasmapause moves inwards, allowing chorus to accelerate electrons to higher energies at comparatively low L-shells, and then outwards, "stranding" this high energy population inside the plasmapause. A particularly dramatic example of this is the recent reports of the "third radiation belt" observed by the Van Allen probes [*Baker et al.*, 2013], and subsequently successfully modeled [e.g. *Thorne et al.*, 2013a]. One should note this sort of dynamical behavior is not uncommon, and can also lead to electron flux enhancements inside the plasmapause at non-relativistic energies [*Lichtenberger et al.*, 2013]. There have also been previous studies reporting links between the plasmapause location and relativistic electron precipitation caused by chorus [e.g. *Johnston and Anderson*, 2010] and EMIC waves [*Carson, Rodger and Clilverd*, 2013].

Lam et al. [2010] observed using the POES (Polar Orbiting Environmental Satellite) >30 keV electron flux that the distribution of precipitating flux in this energy range was well correlated with the global distribution of lower band chorus observed by CRRES (Combined Release and Radiation Effects Satellite). More recent modeling showing the high efficiency of chorus wave particle acceleration *Li et al.* [2013] agrees with this result and was further confirmed with high resolution electron flux measurements from NASA's Van Allen probes [*Thorne et al.*, 2013b]. These observations showed that chorus waves could explain all the observed energy and angular distribution of relativistic electron fluxes in a particular case study.

The POES (Polar Orbiting Environmental Satellite) network of polar orbiting satellites (formerly known as TIROS - Television and InfraRed Observation Satellite) are operated by NOAA (National Oceanic and Atmospheric Administration). These satellites have been running from NOAA-05 in 1978 up to the present in Sun-synchronous orbits at varying Equatorial Crossing Times (ECT). EUMETSAT added the MetOp-02 satellite to the POES network with the same particle instrumentation in May 2007. The MEPED (Medium Energy Proton and Electron Detector) instrument is the focus of our study and the data have been widely used in previous research on electron precipitation [e.g *Callis*, 1997; *Millan et al.*, 2010; *Carson, Rodger and Clilverd*, 2013]. The MEPED instrument is an electron flux detector, which takes measurements at both 0° and 90° pitch angles for 3 integral energy ranges. A full description of the instrument is included in Section 2.1. The main advantage of using this instrument for magnetospheric research comes from the large datasets, which span more than two solar cycles with almost continuous data coverage.

The goal of our study is undertake a superposed epoch analysis of precipitating electron flux so that we can perform fitting techniques to provide an accurate empirical EEP model during geomagnetic storm time. This model can then be used to give an approximate precipitating electron flux inside and outside of the plasmapause due to chorus and plasmaspheric hiss.

2. Data acquisition

To get an average of the electron fluxes around the plasmapause at different geomagnetic conditions we use data collected from the long running POES satellite constellation.

2.1. POES electron flux instrument

The NOAA/POES MEPED sensor provides two kinds of particle count rate measurements including two directional measurements of protons (0.03 to >6.9 MeV, with 6 energy steps labeled P1 to P6) and electrons (0.03-2.5 MeV, in 3 energy ranges, labeled E1 (>30 keV), E2 (>100 keV) and E3 (>300 keV)). There are two telescopes sampling both protons and electrons pointing in different directions, each with a viewing width of $\pm 15°$. The 0° detector is directed along the Earth-spacecraft radial direction, and the axis of the 90° detector is perpendicular to this (anti-parallel to the spacecraft velocity vector). Modeling work has established that the 0° telescope monitors particles in the atmospheric bounce loss cone that will enter the Earth's atmosphere below the satellite when the spacecraft is poleward of L≈1.5-1.6, while the 90° telescope monitors trapped fluxes or those in the drift loss cone, depending primarily upon the L shell [*Rodger et al.*, 2010b, Appendix A].

The MEPED instrument has been updated as part of the SEM-2 subsystem and these changes have been implemented from NOAA-15 to NOAA-19 and the MetOp-2 satellite. For our study we consider only observations made using SEM-2, and hence only the satellites listed above are considered. We use the equations given in *Lam et al.* [2010] to convert from instrument counts to integral electron flux values with units of $\mathrm{cm^{-2}sr^{-1}s^{-1}}$. The *Lam et al.* [2010] equations also remove proton contamination for periods observed outside of the South Atlantic Magnetic Anomaly (SAMA) and solar proton events. A full description of the SEM-2 system which includes the MEPED instrument can be found in *Evans and Greer* [2004].

2.2. MLT and *L* shell data binning

The aim of this paper is to characterize energetic electron fluxes both inside and outside of the plasmapause and to do this we sort our data by Magnetic Local Time (MLT).

Figure 1 is taken from *Summers, Ni and Meredith* [Figure 21, 2007], showing a schematic of the plasmapause location including a drainage plume. The main areas of chorus wave and plasmaspheric hiss activity are also shown, separated by the plasmapause. In this study we have selected two MLT sectors to determine the effects of each wave type, and to characterize the resultant electron precipitation occurring inside and outside of the plasmapause. We identify the regions which are chorus-dominated as spanning 01:00-08:00 MLT (morning) and hiss-dominated as spanning 11:00-16:00 MLT (afternoon). These two regions are shaded in Figure 1 with the grey region showing the morning sector (chorus wave dominated) and the purple region shows the afternoon sector (plasmaspheric hiss dominated). We note that both chorus and hiss regions are more extensive than investigated here, but we use focused regions to identify the main characteristics of the whole region driven by each wave type.

The precipitating electron fluxes measured by the POES 0° pointing telescope between 1999 and 2012 are binned by both IGRF L shell and time with respective resolutions of 0.2 L and 20 minutes for each MLT sector and integral energy range. Observations from inside and around the SAMA are excluded before the measurements are combined. There are 42 bins in L shell ranging from $L = 1.8$ to $L = 10.2$, when discussed in this study each bin will be referred to by its central L shell value (e.g. the first bin is at $L = 1.9$). It should be noted that the lowest L shell considered, $L = 1.8$, is larger than the minimum L shell required to ensure that the 0° MEPED instrument is observing precipitating electrons (Section 2.1). To maximize the quality and MLT range of the electron flux data, results from all available POES satellites are combined and the median taken from the available fluxes in each bin.

3. Determination of storm epochs

To create an average dataset of how electron precipitation varies during geomagnetic storms and the gradual recovery to quiescent conditions, we undertake a superposed epoch analysis for each MEPED energy channel and MLT sector around an identified geomagnetic storm. To begin our investigation we create a superposed epoch dataset ranging from 5 days before to 15 days after a geomagnetic storm allowing both quiet (pre and post storm) and active (storm time) geomagnetic activity to be compared.

While Kp is commonly used in energetic electron studies [e.g., *Meredith et al.*, 2006; *Whittaker et al.*, 2013], Dst is chosen as the geomagnetic index for this study as it is continuous, rather than Kp which has specific discrete values (e.g. 0, 0.3, 0.7, etc), *Simon-Wedlund et al.* [2014] also showed that Dst was a good proxy for EEP flux. Dst is a measure of the energy density of the ring current measured at several equatorial stations around the globe by determining differences in the horizontal component of the Earth's magnetic field [*Sugiura*, 1964] and describes the magnetospheric response to the solar wind *Gonzalez et al.* [1994]. These values are generally negative and we take a value of Dst $\leq$ -50nT as describing geomagnetic stormtime [*Borovsky and Denton*, 2006] with the local minimum used as the epoch point [*Loewe and Prölss*, 1997]. To ensure that a storm only counts once, an extra condition is applied to the Dst detection algorithm. We make sure that each geomagnetic storm begins in a quiet magnetosphere by producing a "clean" list of storms as described by *Katus et al.* [2013]. These authors require a 48 hour period with

Dst > -50 nT before any Dst minimum to ensure a list of well defined, isolated geomagnetic storms. Previous work using DEMETER has shown that geomagnetic storms can affect electron fluxes for longer time periods than this [*Whittaker et al.*, 2013] and so we extend this pre-storm quiet period to 5 days. The total number of acceptable Dst storm epochs identified during the 13 year time period was 164. The POES/MEPED proton data were then checked during each storm event in order to remove any which include Solar Proton Events (SPE). The POES/MEPED electron telescopes are sensitive to proton contamination [*Yando et al.*, 2011] and while a previous study [*Whittaker et al.*, 2014] has shown that the *Lam et al.* [2010] proton removal equations give a good approximation of the true electron flux, the approach fails during solar proton events and inside the SAMA. Hence, we remove any events which MEPED reports as having a differential proton flux >10 $cm^{-2}sr^{-1}s^{-1}keV^{-1}$ in the P5 channel (at an energy of 2.63 MeV) during any time in the epoch. This SPE detection process removed 61 storms. The remaining 103 events were then combined by taking the median flux within each 12 hour time bin and 0.2 L shell bin. The superposed epoch analysis covers 20 days, beginning 5 days before Dst minimum and giving 41 time bins, and is performed for 42 L bins, ranging from $L = 1.8$ to $L = 10.2$.

The left panel of Figure 2 shows the median Dst value taken from these 103 epochs at 12 hour intervals. There is a smooth variation in the Dst values which take approximately 7 days to return to quiet levels (-11 nT) after the storm peaks at zero epoch (median of -61 nT). We use the model Dst equation for the plasmapause location (L_{pp}) given in *O'Brien and Moldwin* [2003]. We note from Table 1 of the O'Brien and Moldwin paper that using the minimum of the 12 or 24 hour Dst value works equally well for the models, so we take the minimum of the Dst in 12 hour resolution. The MLT dependent equation was initially trialed with our dataset, producing L_{pp} values which were higher in L during the morning MLT than during the afternoon MLT sector (consistent with moderate disturbance in Figure 2 of *O'Brien and Moldwin* [2003]). This difference in L is opposite to what would be expected as the model is unable to reproduce either plume structure or the dusk-side bulge that would be expected from such a plume. To recreate the disturbed Dst L_{pp} O'Brien and Moldwin use a Dst of ∼-300 nT, which is an unrealistic index for averaged Dst values to reach. We therefore use the non-MLT plasmapause location equation for this study. The right panels of Figure 2 show the E3 response for the morning and afternoon MLT sectors. The main features of these panels are the precipitation due to chorus (outside the plasmapause from Figure 1) at the epoch time (t = 0) and also the precipitation due to plasmaspheric hiss (inside the plasmapause from Figure 1, t = 2 to 7 days). The solid line in panels b) and c) is the O'Brien and Moldwin model plasmapause for the Dst shown in panel a). This model plasmapause appears to bisect the hiss precipitation leaving a significant amount outside the plasmapause. To compensate for this we provide a constant addition to the model plasmapause within the error limits defined by O'Brien and Moldwin (± 1 L). In panel b) we find that an addition of 0.5 L (dashed line) to the O'Brien and Moldwin L_{pp} values better enclose the hiss precipitation and still leaves the chorus induced precipitation outside of the plasmapause. When we perform the same shift for the afternoon MLT in panel c) we find that a constant addition of 0.75 L performs better at separating the chorus and hiss induced precipitation. This difference is consistent with the schematic shown in Figure 1 and illustrates the problem with the MLT dependent plasmapause equations. We use the +0.5 L addition to the O'Brien and Moldwin L_{pp} plasmapause model for our morning MLT analysis. As we find no plasmapause relation for the hiss precipitation (only averaged Dst) the afternoon plasmapause shift of +0.75 L is only shown for completeness.

4. EEP characteristics outside of the plasmapause

To determine electron precipitation occurring outside the plasmapause we investigate the chorus dominated morning MLT sector of Figure 1 (01:00 - 08:00). Figure 3 shows the variation in EEP fluxes around the storm epoch for all three channels of the MEPED instrument in the morning MLT sector, >30 keV (top left panel), >100 keV (top right panel) and >300 keV (lower left panel). A power law fit, previously shown to be the best type of electron spectral fit to apply [*Whittaker et al.*, 2013], is applied to each L shell and time bin across the three energies. The spectral index of this fit is shown in the lower right panel of Figure 3. The chorus induced electron flux is observed outside the plasmapause with the enhancement in flux lasting approximately 7 days. The hiss induced precipitation can be seen clearly in the >300 keV channel inside the plasmapause.

The fitting of the flux in the three integral electron channels is performed by applying a linear fit to the $\log_{10}$ of the energy and flux values (Equation (1)), giving a power law fit on linear axes (Equation (2)) as shown below. The fit spectral index is always negative as we are fitting integral energy ranges (i.e., >100 keV channel has to have lower fluxes than the >30 keV channel).

$$log_{10}j = \gamma log_{10}E + log_{10}\alpha \tag{1}$$

$$j = \alpha E^{\gamma} \tag{2}$$

Where:

$$j = \text{integral flux at energy E } (\text{cm}^{-2}\text{sr}^{-1}\text{s}^{-1})$$

The previously described plasmapause location fits extremely well to the fluxes of all three energies, describing the boundary between high and low precipitating fluxes. To provide information on precipitating fluxes outside the plasmapause we provide two simulations; > 30 keV and the power law fit spectral index. The ability to reproduce both of these parameters will allow precipitating electron fluxes of any energy to be calculated relative to the plasmapause location as a geomagnetic storm progresses.

4.1. >30 keV simulation process

We begin by investigating the >30 keV superposed epoch (top left panel of Figure 3). The data shows that the highest precipitating fluxes are in the 12 hour bin around storm time, meaning that no delay between Dst and flux needs to be incorporated. This matching of peak electron flux to the Dst minimum indicates that the precipitation due to chorus wave interaction occurs within 6 hours of the main phase of the storm.

At each 12 hour time frame of the >30 keV data we plot the precipitating electron flux as a function of the distance from the plasmapause (S_{pp}) and apply a Gaussian fit in the form of Flux $= a.e^{-\left(\frac{S_{pp}-c}{w}\right)^2}$. These fits produced an average adjusted r^2 (r$^2_{\text{adj}}$) value of 0.87 with the lowest correlations (∼0.81) occurring at the maximum Dst plateau before the storm. The variables (a, c and w), which were different at each time frame, were then compared to the corresponding absolute Dst value and fitted with simple functions. The final equation for simulating the >30 keV is shown in Equation (3) providing flux with units of $e^{-}cm^{-2}sr^{-1}s^{-1}$.

$$\mathrm{Flux}_{chorus} = a(|Dst|).e^{-\left(\frac{S_{pp}-c(|Dst|)}{w(|Dst|)}\right)^2} \tag{3}$$

where:

$$a(|Dst|) = 4.53|Dst|^{2.475}$$

$$c(|Dst|) = 3.11|Dst|^{-0.14}$$

$$w(|Dst|) = 1.59.e^{-0.061|Dst|} + 0.95$$

$$S_{pp} = \text{distance from the plasmapause (in } L\text{)}$$

The blue solid lines in the left panels of Figure 4 show time varying plots of the superposed epoch analyzed precipitating flux at 4 different distances from the plasmapause. These distances start at the plasmapause location and increase to 3 L outside the plasmapause. The black dashed lines in this figure show the average precipitating flux before the storm at each distance from the plasmapause, and it can be seen that the fluxes take approximately 7 days to recover, on a similar timescale to Dst. Equation (3) was then tested by simulating the flux seen at each distance from the plasmapause and has been included as the red dashed line in the left panels of Figure 4, the simulation also has a minimum flux condition applied (to match the instrument noise) which is described in Section 4.3 and only affects the value at 12 hours before the storm. These model fluxes match very well to the lines representing observed flux outside the plasmapause (linear correlation coefficient > 0.95) but less well at the plasmapause (linear correlation coefficient of 0.87), with root mean squared error (RMSE) values of 391 (L_{pp}), 2600 (L_{pp} + 1), 2589 (L_{pp} + 2) and 1180 $cm^{-2}sr^{-1}s^{-1}$ (L_{pp} + 3). A full simulation of Equation 4 is discussed in Section 4.3. We conclude that this equation performs adequately in modeling the >30 keV precipitating electron fluxes outside the plasmapause.

4.2. Flux spectral index simulation

We now investigate the electron flux spectral index (γ) for the varying geomagnetic conditions shown in the lower right panel of Figure 3. This is performed in a similar way to the >30 keV flux simulation in Section 4.1.

The spectral index is compared to the distance from the plasmapause for each of the 12 hour time bins. Unlike the >30 keV fitting, a single Gaussian fits poorly. This poor fit arises from a sharp change in spectral index at low L shells (e.g., L = 3.1 (-0.29) to L = 4.3 (-2.25)), at higher L the increase from minimum takes place over a larger L space (e.g., L = 5.5 (-2.89) to L = 6.7 (-2.13) over the same distance in L). Hence, a double Gaussian was required to accurately simulate the high L response. To be able to fit the coefficients of the double Gaussian as a function of Dst we had to include restrictions to the spectral index vs plasmapause distance fit. The first condition was to lock the centre of the first Gaussian to the minimum index value and the second condition was to make sure the centre of the second Gaussian was at a higher L value than the first centre. These conditions ensured a smooth shape and the ability to sensibly fit the coefficients to the absolute Dst value. The full equation is shown in Equation 4.

$$\gamma_{chorus} = a_1(|Dst|).e^{-\left(\frac{S_{pp}-c_1(|Dst|)}{w_1(|Dst|)}\right)^2} + a_2(|Dst|).e^{-\left(\frac{S_{pp}-c_2(|Dst|)}{w_2(|Dst|)}\right)^2} \quad (4)$$

where:

$$a_1(|Dst|) = -3.8 \times 10^4 |Dst|^2 - 0.0142|Dst| - 0.12 \quad a_2(|Dst|) = 1.14.e^{-0.092|Dst|} - 1.4$$

$$w_1(|Dst|) = 6.123|Dst|^{-0.34} \quad w_2(|Dst|) = 3.66$$

$$c_1(|Dst|) = -0.0126|Dst| + 2.074 \quad c_2(|Dst|) = 0.03|Dst| + 2.6$$

$$S_{pp} = \text{distance from the plasmapause (in L)}$$

The right panels of Figure 4 show the observed (solid blue) and simulated (dashed red) spectral index for 4 distances from the plasmapause in a similar style to the left hand panels. The thin dashed black line indicates the average spectral index before the storm. The minimum in spectral index again occurs in the 12 hours around the Dst minimum, with a similar 7 day recovery time. The spectral indicies calculated from Equation (4) again show an excellent fit outside the plasmapause with +1 and +2 L from the plasmapause having linear correlation coefficients > 0.9 (RMSE values are 0.231 and 0.129 respectively). The simulation of the spectral index at +3 L slightly overestimates the data with a linear correlation coefficient of 0.87 (RMSE = 0.254). The simulation at the plasmapause again overestimates the data with the day before the storm particularly different from the data. The linear correlation coefficient for this plot is 0.64 (RMSE = 0.346). A full simulation of Equation (4) is discussed in Section 4.3. We conclude this equation performs adequately in modeling the spectral index of precipitating electron fluxes outside the plasmapause.

4.3. Model confidence

Examination of Figure 4 shows very clearly that the equations do an excellent job of reproducing the fluxes and spectral index outside the plasmapause. Taking 1 L outside the plasmapause as an example, the average >30 keV flux difference between the model and observations is 2600 $cm^{-2}sr^{-1}s^{-1}$ with an interquartile range of 691, giving a range of between 2×10^3 and 3×10^3 (this average value is 2.3% of the storm time flux). This range is approximately equal to the average flux during quiet geomagnetic conditions (shown by the dashed black line). Performing a similar analysis for the spectral index at 1 L outside the plasmapause gives a mean absolute difference of 0.23 with an interquartile range of 0.2, resulting in an error up to a maximum of 0.43, which is small compared to the data values.

As a more complete test of these equations, the >30 keV and spectral index epoch panels from Figure 3 are recreated using Equations (3) and (4). These are shown in Figure 5 with the >30 keV flux variation shown in the left panels, and the spectral index variation shown in the right panels. When we consider the >30 keV flux epoch, the simulation (middle left panel) looks very similar to the data (top left panel). The biggest source of difference exists in the quiet period before the storm, where the simulation reports fluxes close to zero and the data gives a maximum flux around 10^3 $cm^{-2}sr^{-1}s^{-1}$. There is a background flux in the data which appears to be L shell dependent and we can replicate this by determining the minimum flux value at each L shell and fitting a function to it (shown below in Equation 5). This extra background is unlikely to be representative of the true precipitating flux and is more likely to be the result of instrument noise and is only used when comparing to the MEPED instrument fluxes. The simulation with this minimum flux condition applied is shown in the bottom left panel of Figure 5 and looks extremely similar to the data in the top left panel. An analysis of the difference in data points shows that on average the data is higher than the simulation by less than a factor of 2 (1.73). It should be noted that the biggest errors are at the very high L shell values ($L > 8$).

$$\text{Minimum Flux} = 789.e^{-\left(\frac{L-7.7}{1.9}\right)^2} + 100 \quad (5)$$

When we apply the same analysis of Figure 5 to the spectral index simulation (middle right panel) and data (upper right panel) we again see strong similarities between the two. The largest difference between data and simulation is again the day before the storm and at high L values ($L > 9$). A similar maximum spectral index as a function of L shell is calculated and applied (shown in the lower right panel of Figure 5). The difference between the plots is negligable and the only effect is at the 24 hour period before the storm. We therefore base our comparison between simulation and data using Equation (4) only. The spectral index simulation overestimates the data by a factor of 1.4 on average, this is mostly due to the high L values and the 24 hours on the eve of the storm.

The simulations in Figure 5 also show that at the highest L shells, the simulations do not seem to represent the epoch very well. We therefore advise that the model equations are not used beyond $L = 8.5$, corresponding to approximately 3 L outside the geomagnetically quiet plasmapause.

5. EEP characteristics inside the plasmapause

To determine electron precipitation occurring inside the plasmapause we investigate the plasmaspheric hiss dominated MLT sector (11:00 - 16:00). Figure 6 shows the electron precipitation variation after a superposed epoch analysis for all three channels of the MEPED instrument, >30 keV (top left panel), >100 keV (top right panel) and >300 keV (lower left panel) in a similar manner to Figure 3 and using the same color scales. In comparison to Figure 3 the fluxes outside the plasmapause in the afternoon MLT sector are lower in magnitude. This weaker chorus is a result of insufficient electron flux and anisotropy to drive chorus generation past 15:00 MLT [*Bortnik, Thorne and Meredith*, 2007], with a significant weakening of the chorus past noon as seen in Figure 1. The >300 keV electron fluxes inside the plasmapause are higher than observed in the morning MLT sector, this indicates that our chosen MLT sectors are behaving as expected.

5.1. Energetic distribution of hiss induced precipitation

In Figure 3 the energy spectra of the chorus induced electron precipitation is easily observed. However, this is more difficult inside the plasmapause for the afternoon MLT sector. Examination of Figure 6 shows that the center of the >300 keV channel flux distribution occurs in the bin 84 hours (± 6 hours) after the main phase of the storm at $L = 4.1$. This flux enhancement is very difficult to see in the other integral energy channels even with a narrow color table range indicating there is a lack of any obvious flux enhancement inside the plasmapause in the >30 keV and >100 keV energy channels at this specific time. The >100 keV channel shows some small precipitation enhancement approximately 36 to 72 hours from the main phase of the storm peaking at an L shell of 4.5. There is no visible effect in the >30 keV channel. This is consistent with the results from *Summers, et al.* [2008] stating that electron loss due to pitch angle scattering from plasmaspheric hiss is energy dependent. The typical precipitation time given by these authors states that 100 to 200 keV electrons are lost in approximately one day. For the >30 keV channel this suggests the losses happen much faster and are probably hidden in our observations by the 12 hour time resolution, with the main hiss induced loss happening at the epoch time and visually lost amongst the chorus induced precipitation.

As a further test of these results we investigate the P6 proton channel on the MEPED instrument. The geometric factor related to this high energy proton telescope (>6.9 MeV protons) indicates that it functions very well as a relativistic electron detector when such protons are not present [*Yando et al.*, 2011]. It should be noted that there are no high energy protons present in our analysis as we have removed such epochs as part of our SPE removal. The superposed epoch analysis of this telescope in the afternoon MLT sector is shown in the lower right panel of Figure 6 with the same $\log_{10}$ color scale as the >300 keV channel. The main precipitating flux can be seen at approximately 120 hours from the main phase of the storm with a narrower L shell profile and centered at a lower L shell (L = 4.2) than the >300 keV precipitation. The energy of this channel has been determined in previous studies as approximately >800 keV [e.g. *Carson, Rodger and Clilverd*, 2013; *Rodger et al.*, 2010b], as this is when the geometric factor for the electrons in this channel is greater than 10^{-3} cm^2 sr. We can also make an estimate of the upper energy limit. From the geometric factors given in *Yando et al.* [2011], the P6 channel would respond more strongly than the >300 keV for electrons above 1.4 MeV. Thus, as the fluxes in the P6 channel are lower than the >300 keV channel from Figure 6, we can assume the energy of a high proportion of precipitating electrons detected in the P6 channel are between 0.8 and 1.4 MeV.

An interesting point of note is that there is no evidence of chorus induced precipitation in the P6 observations. The morning MLT superposed epoch analysis was also investigated and showed the same lack of precipitating flux outside the plasmapause. *Horne, Lam* *and Green* [2009] showed that electrons with energies >1 MeV are not precipitated but scattered into the drift loss cone and lost around the SAMA. As we have removed the SAMA geographical location from our superposed epoch analysis then it is consistent that we see no precipitating flux with energy greater than 800 keV outside the plasmapause.

5.2. Hiss induced EEP simulation (>300 keV)

We now proceed to simulate the fluxes inside the plasmapause. From our observations we can only simulate the >300 and >800 keV (P6) channels and we begin with the >300 keV observations.

The method used to characterize the chorus induced >30 keV precipitation and spectral index can not be used in this case as it is clear that the flux inside the plasmapause does not follow the Dst value directly, (i.e., there is no sharp cut off between pre and post storm). Providing a delay in the Dst does not assist the analysis due to the rapid change in plasmapause location and gradual change in >300 keV flux. However, by taking an average of |Dst| over the previous 84 hours provides an index that gradually increases to maximum and then gradually returns to background levels, in a similar manner to the >300 keV flux inside the plasmapause. We also observed that the distribution of flux does not appear to change in L shell. Our method of simulation is then to take rows of the data array corresponding to L shell, fitting them to the averaged |Dst| value described above. The fit appears to follow a power law with a constant gradient value of 0.055. The amplitude is fitted to L with a Gaussian and the full equation providing >300 keV electron flux with units of cm^{-2}sr^{-1}s^{-1}, is shown below in Equation (6).

$$\mathrm{Flux}_{\mathrm{hiss}>300} = \mathrm{a(L)}|\overline{\mathrm{Dst}}_{-84:0}|^{0.055} \tag{6}$$

where:

$$a(L) = 128e^{-\left(\frac{L-4.5}{3.2}\right)^2}$$

A selection of the >300 keV flux lines can be seen in panels a) to d) of Figure 7 as the solid blue line. The fluxes are taken at $L = 3.9$ (panel a), $L = 4.5$ (panel b), $L = 4.9$ (panel c) and $L = 5.3$ (panel d). The dashed red line on each panel is the simulation calculated from Equation (6) at each L. It should be noted that panels b) to d) strongly underestimate the observations at the zero epoch. This is intentional as these L shells have precipitation induced from chorus waves at this time which we do not wish to include. If we ignore the zero epoch time, the largest difference between the simulation and data in these panels is $\sim$10 cm^{-2}sr^{-1}s^{-1}, this occurs at the minimum flux value ($L = 4.9$, $t = +12$ days) and contributes 8% of this flux.

Panel e) of Figure 7 shows the >300 keV epoch from Figure 6 on a linear color scale, with the plasmapause shown as the black dashed line. We then use Equation (6) to attempt to replicate panel e). The simulation is shown in panel f) utilizing the same color scale. Using the 84 hour averaged Dst gives a simulation which appears to agree well by eye. We compare the simulation and the observed data between $2.5 \leq L \leq 5.9$ and between -1.5 days $\leq t \leq +15$ days with the 12 hour zero epoch removed. The mean absolute difference between these arrays is 6.2 cm^{-2}sr^{-1}s^{-1} which is 4% of the average flux in this region (137 cm^{-2}sr^{-1}s^{-1}) and 16% of the range between the minimum (120 cm^{-2}sr^{-1}s^{-1}) and maximum (158 cm^{-2}sr^{-1}s^{-1}) flux.

5.3. Hiss induced EEP simulation (>800 keV)

As we have simulated the >300 keV channel we now move onto a simulation of the >800 keV (P6) channel. The superposed epoch of the >800 keV channel in Figure 6 (lower right panel) is visually very similar to the >300 keV superposed epoch (lower left panel). The main differences between them are the L shell range of precipitating electrons and the time lag with respect to average Dst, as previously mentioned. We therefore apply the same simulation technique as used for the >300 keV electron channel (Section 5.2) to the P6 observations.

The superposed epoch of the >800 keV precipitating electrons is reproduced in panel (g) of Figure 7 shown using a linear color scale. The superposed epoch analysis flux value at each 0.2 L shell between $L = 3.3$ and $L = 5.5$ is taken and compared to the mean Dst value from 5 days to 1 day previously. The data was tested using the 5 day Dst mean and the fitting did not perform as well as the 4 day average Dst with a 24 hour delay. The fitting equation produced is in the same form as Equation (6), with the same power index value of 0.055 used. The amplitude of the power fit is then calculated with a fitted Gaussian and the coefficients are given below in Equation (7).

$$\mathrm{Flux}_{\mathrm{hiss}>800} = \mathrm{a(L)}|\overline{\mathrm{Dst}}_{-120:-24}|^{0.055} \tag{7}$$

where:

$$f(L) = 114e^{-\left(\frac{L-4.2}{2.8}\right)^2}$$

The simulation of the time variation of the P6 fluxes is shown in panel h) of Figure 7 and on the same color scale as the superposed epoch analysis observations in panel g). When we compare the differences between the observations and the simulation ($2.9 \leq L \leq 5.5$,

$t \geq 0$), we find that the mean difference (using absolute values) is 3.3 cm^{-2}sr^{-1}s^{-1} which is 2.8% of the average flux in this region (122 cm^{-2}sr^{-1}s^{-1}) and 8% of the range between the minimum (100 cm^{-2}sr^{-1}s^{-1}) and maximum (143 cm^{-2}sr^{-1}s^{-1}) flux.

6. Discussion

We now have a complete model description of the POES observed electron fluxes outside and inside the plasmapause due to chorus and plasmaspheric hiss. As a confirmation of our results we investigate the DEMETER (Detection of Electro-Magnetic Emissions Transmitted from Earthquake Regions) ICE (Instrument Champ Electrique) instrument observations to determine the wave activity in the lower chorus band using our superposed epoch analysis. The ICE instrument performs a continuous survey of a wide range of DC and AC electric fields with a high sensitivity and a 1 second temporal resolution. A full description of the instrument can be found in *Berthelier et al.* [2006]. A previous study [*Hayosh et al.*, 2013] has linked electron precipitation to chorus wave activity using ICE and POES data in two case studies. Panel a) of Figure 8 shows a superposed epoch analysis using the same epochs as we used for the POES analysis, but limited to those which occurred in the DEMETER satellite lifetime of 2006-2011. The limitation of requiring an isolated storm means that the epochs within this time period (around solar minimum) are limited to 16 events. The model plasmapause, as calculated in Section 3 for the morning MLT, is included as the dashed line on this plot. The color scale indicates the variation in the power of lower band chorus waves. This plot shows that the chorus wave activity peaks at storm time and is largely contained outside of the plasmapause. This confirms that strong chorus wave activity is present during the main period when the electron precipitation is enhanced. Note also that there is enhanced wave power inside the plasmapause for some days after the storm time zero epoch. This is likely to be caused by plasmaspheric hiss, which can overlap the frequency band of lower-band chorus in that L shell range. The modeling study of *Chen et al.* [2012] showed that this hiss response is likely formed by chorus emissions originating at low L during the inward movement of plasmapause location.

To visually show the difference in electron flux enhancement effects between chorus and hiss we plot both observations together with the Dst value. Panel b) of Figure 8 shows the peak electron flux for each wave type (>30 keV for chorus and >300 keV for hiss). The chorus precipitating flux is shown as the blue solid line with circles, occurs at L = 5.5 and has a peak electron flux of 1.24×10^5 cm^{-2}sr^{-1}s^{-1}. The peak hiss precipitating flux occurs at L = 4.5 and is shown by the green solid line with x markers, the maximum flux at this L shell is 158 cm^{-2}sr^{-1}s^{-1}. The Dst value is also shown as the black dashed line for comparison. The relative difference in precipitating electron enhancements is very clear in this figure with the chorus having an effect over three orders of magnitude larger than hiss. This is an expected result as the average population of >30 keV electrons is much larger than the average population of >300 keV electrons. A comparison of the strength of the effects of chorus and hiss can be found by comparing the peak >300 keV flux inside and outside of the plasmapause. The peak flux outside of the plasmapause for the >300 keV morning MLT precipitating electrons is 187 cm^{-2}sr^{-1}s^{-1} and the peak inside the plasmapause is 158 cm^{-2}sr^{-1}s^{-1}. When we consider these fluxes as enhancements from the background flux value (100 cm^{-2}sr^{-1}s^{-1}) we find that the chorus induced enhancement has an effect approximately 1.5 times stronger than the hiss induced enhancement. Evidently this is only true for high energy electrons, as fluxes that are a factor of $\frac{2}{3}$ of the peak chorus induced flux inside the plasmasphere would be clearly visible in Figures 3 and 6 at lower energies. Panel c) of Figure 8 shows just the hiss peak flux on a much reduced and linear y-axis range. The Dst delay effect can be clearly seen as well as the small chorus contamination effect at the time of the storm. The purple dashed line with + markers in this plot represents the previous 3.5 day mean Dst, to show the similarity between this index and the flux.

The P6 channel (>800 keV) in the afternoon MLT epoch shows a flux drop out at storm onset. This is commonly seen in high energy electron fluxes during geomagnetic activity and is a result of radial outward transport of electrons through the magnetopause [*Turner et al.*, 2012]. The flux then returns strongly around L shells of 3.5 to 5.5, this matches well with the observations seen in *Horne et al.* [2005]. However, the work by these authors attributed the high energy relativistic flux to chorus acceleration just outside the plasmapause, increasing the flux by an order of magnitude approximately 24 hours later. We attribute our observed precipitation (with an approximate 10% increase from quiet time) to plasmaspheric hiss which peaks in wave power at $L = 4.4$ [*Li et al.*, 2014].

Our epochs have been created using the 1 hour median Dst value from each event in the statistical model we have created, this means that our equations have not included any positive Dst values. When used for comparison in case studies this is important as the effects of Dst > 0 on the model are unknown. This is especially true in the case of the >30 keV flux which uses the absolute value of Dst and hence a positive Dst would increase the model precipitation level, rather than reduce it as would be expected.

7. Conclusions

We have performed a superposed epoch analysis of precipitating electron flux taken from the POES/MEPED instrument. The epoch has been based on the minimum value of Dst during a geomagnetic storm, taken when Dst drops below -50 nT with a previous 5 day quiet period. Our results have been split into two MLT regions to focus upon the different enhancement effects of chorus and plasmaspheric hiss waves on the electron precipitation. From our superposed epoch analysis we have shown that for the morning MLT sector, the precipitating electron fluxes outside the plasmapause are greatly enhanced during storm time with this flux correlating strongly with the Dst value and distance from the modeled plasmapause location. In contrast, the noon/afternoon MLT sector shows time varying precipitating electron flux inside the plasmapause dependent upon electron energy. The >300 keV channel precipitation peak occurs 84 hours after the minimum Dst value, while the relativistic electron (>800 keV) precipitation peak occurs 120 hours after the main phase of the storm. Neither hiss induced precipitation profile is dependent upon the plasmapause position.

By taking electron flux values as a function of distance from the modeled plasmapause, we have produced a model description of the enhancements in flux for the morning MLT sector associated with chorus wave interaction. The >30 keV electron flux model is given in Equation 3, along with the modeled power law fit spectral index response in Equation 4. The combination of these two equations allows us to model the full precipitating electron energy response during a geomagnetic storm outside the plasmapause, valid up to $L = 8.5$. We have also observed that electrons >800 keV are very unlikely to precipitate outside the plasmapause within our MLT sectors and L shell ranges.

The electron flux enhancements inside the plasmapause in the afternoon MLT sector, associated with plasmaspheric hiss, have been modeled for electrons with energies above 300 keV. The >300 keV model, shown in Equation 6, depends on the L shell and operates on a mean of the Dst values over the previous 3.5 days (inclusive of the current time bin). The simulation of the P6 channel fluxes (Equation (7)) also depend on L shell and relies on a mean 96 hour Dst value with a 1 day lag, both consistent with the results of *Summers, et al.* [2008].

The models we have produced can be used to estimate precipitating electron fluxes based on real time estimates of Dst and plasmapause location. The European Union FP7 funded project PLASMON, intends to assimilate near real time measurements of plasmaspheric densities into a dynamic plasmasphere model using whistler waves detected by a VLF ground network (e.g. *http://plasmon.elte.hu/*, *Collier et al.* [2011], *Lichtenberger et al.* [2013]). This project complements our EEP precipitation model equations providing values which can be compared both to satellite measurements (POES, DEMETER and the more recent Radiation Belt Storm Probes missions) and ground based VLF perturbations (e.g. AARDDVARK network, *http://www.physics.otago.ac.nz/space/AARDDVARK_homepage.htm*). The combination of the plasmapsheric results from PLASMON and our model will allow a near real-time estimate to be made of precipitating energetic electron fluxes.

Acknowledgments. The research leading to these results has received funding from the European Community's Seventh Framework Programme ([FP7/2007-2013]) under grant agreement number 263218. The authors wish to thank the NOAA personnel who developed, maintain, and operate the NOAA/POES spacecraft. The data used in this paper are available at NOAA's National Geophysical Data Center (NGDC - NOAA 15-19 and MetOp-02 MEPED data).

References

Andersson, M., P. T. Verronen, S. Wang, C. J. Rodger, M. A. Clilverd, and B. R. Carson (2012), Precipitating radiation belt electrons and enhancements of mesospheric hydroxyl during 20042009., *J. Geophys. Res.*, *117*(D09304), doi:10.1029/2011JD017246.

Andersson, M., P. T. Verronen, C. J. Rodger, M. A. Clilverd, and S. Wang (2014), Longitudinal hot-spots in the mesospheric OH variations due to energetic electron precipitation, *Atmos. Chem. Phys.*, *4*, doi:10.5194/acp-14-1095-2014.

Baker D. N., S. G. Kanekal, V. C. Hoxie, M. G. Henderson, X. Li, H. E. Spence, S. R. Elkington, R. H. W. Friedel, J. Goldstein, M. K. Hudson, G. D. Reeves, R. M. Thorne, C. A. Kletzing, S. G. Claudepierre (2013), A Long-Lived Relativistic Electron Storage Ring Embedded in Earths Outer Van Allen Belt, *Science*, 340(6129), doi:10.1016/science.1233518.

Berthelier, J. J., M. Godefroy, F. Leblanc, M. Malingre, M. Menvielle, D. Lagoutte, J.Y. Brochot, F. Colin, F. Elie, C. Legendre, P. Zamora, D. Benoist, Y. Chapuis, J. Artru, and R. Pfaff (2006), ICE, the electric field experiment on DEMETER, *PSS*, 54(5), doi:10.1016/j.pss.2005.10.016.

Borovsky, J. E., and M. H. Denton (2006), Differences between CME driven storms and CIR driven storms, *J. Geophys. Res.*, 111, A07S08, doi:10.1029/2005JA011447.

Bortnik, J., R. M. Thorne, and N. P. Meredith (2007), Modeling the propagation characteristics of chorus using CRRES suprathermal electron fluxes, *J. Geophys. Res.*, *112*, doi:10.1029/2006JA012237.

Brasseur, G., and S. Solomon (2005), *Aeronomy of the Middle Atmosphere, third ed.*, D. Reidel Publishing Company, Dordrecht.

Callis, L. B. (1997), Odd nitrogen formed by energetic electron precipitation as calculated from TIROS data, *Geophys. Res. Lett.*, *24*(24), doi:10.1029/97GL03276

Carson, B., C. J. Rodger and M. A. Clilverd (2013), POES satellite observations of EMIC-wave driven relativistic electron precipitation during 1998-2010, *J. Geophys. Res.*, *118*, doi:10.1029/2012JA017998.

Chen, L., J. Bortnik, W. Li, R. M. Thorne and R. B. Horne (2012), Modeling the properties of plasmaspheric hiss: 1. Dependence on chorus wave emission, *J. Geophys. Res.*, *117*, doi:10.1029/2011JA017201.

Collier, A. B., J. Lichtenberger, M. Clilverd, B. Heilig, M. Vellante, J. Manninen, C. J. Rodger, A. Jorgensen, J. Reda, R. Holzworth, R. Friedel, (2011), PLASMON: Data assimilation of the Earth's plasmasphere, *General Assembly and Scientific Symposium, 2011 XXXth URSI*, 13-20 Aug. 2011, doi:10.1109/URSIGASS.2011.6051134.

Evans, D. S., and M. S. Greer (2004), Polar orbit environmental space satellite space environment monitor 2: Instrument description and archived data documentation v1.3, *NOAA Technical Memorandum, Space Environ. Lab., Boulder, Colorado*

Gonzalez, W. D., J. A. Joselyn, Y. Kamide, H. W. Kroehl, G. Rostoker, B. T. Tsurutani and V. M. Vasyliunas (1994), What is a Geomagnetic Storm?, *J. Geophys. Res.*, *99*, doi:10.1029/93JA02867.

Hayosh M., D. L. Pasmanik, A. G. Demekhov, O. Santolik, M. Parrot and E. E. Titova (2013), Simultaneous observations of quasi-periodic ELF/VLF wave emissions and electron precipitation by DEMETER satellite: A case study, *J. Geophys. Res.*, *118*, doi:10.1029/jgra.50179.

Helliwell R. A. (1969), Low-frequency waves in the magnetosphere, *Rev. Geophys.*, *7*, doi:10.1029/RG007i001p00281.

Hikishima, M., Y. Omura and D. Summers (2010), Microburst precipitation of energetic electrons associated with chorus wave generation, *Geophys. Res. Lett.*, *37*, doi:10.1029/2010GL042678.

Horne, R. B., and R. M. Thorne (1998), Potential waves for relativistic electron scattering and stochastic acceleration during magnetic storms, *Geophys. Res. Lett.*, *25*, doi:10.1029/98GL01002.

Horne, R. B., R. M. Thorne, S. A. Glauert, J. M. Albert, N. P. Meridith, and R. R. Anderson (2005), Timescales for radiation belt electron acceleration by whistler mode chorus waves, *J. Geophys. Res.*, *110*, doi:10.1029/2004JA010811.

Horne, R. B., M. M. Lam and J. C. Green (2009), Energetic electron precipitation from the outer radiation belt during geomagnetic storms, *Geophys. Res. Lett.*, *36*, doi:10.1029/2009GL040236.

Johnston, W. R. and P. C. Anderson (2010), Storm time occurrence of relativistic electron microbursts in relation to the plasmapause, *J. Geophys. Res.*, *115*(A02205), doi:10.1029/2009JA014328.

Katus, R., M. W. Liemohn, D. L. Gallagher, A. Ridley, and S. Zou (2013), Evidence for potential and inductive convection during intense geomagnetic events using normalized superposed epoch analysis., *J. Geophys. Res.*, *118*, doi:10.1029/2012JA017915.

Lam M. M., R. B. Horne, N. P. Meredith, S. A. Glauert, T. Moffat-Griffin and J. C. Green (2010), Origin of energetic electron precipitation >30 keV into the atmosphere., *J. Geophys. Res.*, *115*(A00F08), doi:10.1029/2009JA014619.

Lakhina G. S., B. T. Tsurutani, O. P. Verkhoglyadova and J. S. Pickett (2010), Pitch angle transport of electrons due to cyclotron interactions with the coherent chorus subelements, *J. Geophys. Res.*, *115*(A00F15), doi:10.1029/2009JA014885.

Li, X., D. N. Baker, T. P. O'Brien, L. Xie, and Q. G. Zong (2006), Correlation between the inner edge of outer radiation belt electrons and the innermost plasmapause location, *Geophys. Res. Lett.*, *33*(L14107), doi:10.1029/2006GL026294.

Li, W., B. Ni, R. M. Thorne, J. Bortnik, J. C. Green, C. A. Kletzing, W. S. Kurth and G. B. Hospodarsky (2013), Constructing the global distribution of chorus wave intensity using measurements of electrons by the POES satellites and waves by the Van Allen Probes, *Geophys. Res. Lett.*, *40*(17), doi:10.1002/grl.50920.

Li, W., B. Ni, R. M. Thorne, J. Bortnik, Y. Nishimura, J. C. Green, C. A. Kletzing, W. S. Kurth, G. B. Hospodarsky, H. E. Spence, G. D. Reeves, J. B. Blake, J. F. Fennell, S. G. Claudepierre and X. Gu (2014), Quantifying hiss-driven energetic electron precipitation: A detailed conjunction event analysis, *Geophys. Res. Lett.*, *41*(4), doi:10.1002/2013GL059132.

Lichtenberger, L., M. A. Clilverd, B. Heilig, M. Vellante, J. Manninen, C. J. Rodger, A. B. Collier, A. M. Jørgensen, J. Reda, R. H. Holzworth, R. Friedel and M. Simon-Wedlund (2013), The plasmasphere during a space weather event: first results from the PLASMON project, *J. Space Weather Space Clim*, *3*(A23), doi:10.1051/swsc/2013045.

Loewe, C. A., and G. W. Prölss (1997), Classification and mean behavior of magnetic storms, *J. Geophys. Res.*, 102(A7), doi:10.1029/96JA04020.

Lyons, L. R., and R. M. Thorne (1973), Equilibrium structure of radiation belt electrons, *J. Geophys. Res.*, *78*(13), doi:10.1029/JA078i013p02142

Meredith, N. P., R. B. Horne, D. Summers, R. M. Thorne, R. H. Iles, D. Heynderickx and R. R. Anderson (2002), Evidence for acceleration of outer zone electrons to relativistic energies by whistler mode chorus, *Annales Geophysicae*, 20, doi:10.5194/angeo-20-967-2002.

Meredith, N. P., R. B. Horne, S. A. Glauert, R. M. Thorne, D. Summers, J. M. Albert, and R. R. Anderson (2006), Energetic outer zone electron loss timescales during low geomagnetic activity, *J. Geophys. Res.*, 111, A05212, doi:10.1029/2005JA011516.

Meredith, N. P., R. B. Horne, M. M. Lam, M. H. Denton, J. E. Borovsky and J. C. Green (2011), Energetic electron precipitation during high-speed solar wind stream driven storms, *J. Geophys. Res.*, 116, A05223, doi:10.1029/2010JA016293.

Millan, R. M, K. B. Yando, J. C. Green, and A. Y. Ukhorskiy (2010), Spatial distribution of relativistic electron precipitation during a radiation belt depletion event., *Geophys. Res. Lett.*, *37*(L20103), doi:10.1029/2010GL044919.

Newnham, D. A., P. J. Espy, M. A. Clilverd, C. J. Rodger, A. Seppälä, D. J. Maxfield, P. Hartogh, K. Holmén, and R. B. Horne (2011), Direct observations of nitric oxide produced by energetic electron precipitation in the antarctic middle atmosphere, *Geophys. Res. Lett.*, *38*(20), L20,104, doi:10.1029/2011GL049199.

O'Brien, T. P., and M. B. Moldwin (2003), Empirical plasmapause models from magnetic indices, *Geophys. Res. Lett.*, 30, 1152, doi:10.1029/2002GL016007.

Rodger, C. J., M. A. Clilverd, N. R. Thomson, R. J. Gamble, A. Seppälä, E. Turunen, N. P. Meredith, M. Parrot, J-A. Sauvaud and J-J Berthelier (2010), Radiation belt electron precipitation into the atmosphere: recovery from a geomagnetic storm, *J. Geophys. Res.*, *112*, A11307, doi:10.1029/2007JA012383.

Rodger, C. J., M. A. Clilverd, A. Seppälä, N. R. Thomson, R. J. Gamble, M. Parrot, J-A. Sauvaud and T. Ulich (2010), Radiation belt electron precipitation due to geomagnetic storms: significance to middle atmosphere ozone chemistry, *J. Geophys. Res.*, *115*, A11320, doi:10.1029/2010JA015599.

Rodger, C. J., M. A. Clilverd, J. Green, and M. Lam (2010), Use of POES SEM2 observations to examine radiation belt dynamics and energetic electron precipitation in to the atmosphere, *J. Geophys. Res.*, *115*, doi:10.1029/2008JA014023.

Seppälä, A., H. Lu, M. A. Clilverd, and C. J. Rodger (2013), Geomagnetic activity signatures in wintertime stratosphere wind, temperature and wave response, *J. Geophys. Res.*, *118*, doi:10.1002/jgrd50236.

Solomon, S., P. J. Crutzen, and R. G. Roble (1982), Photochemical coupling between the thermosphere and the lower atmosphere: 1. Odd nitrogen from 50 to 120 km, *J. Geophys. Res.*, *87*, doi:10.1029/JC087iC09p07206.

Sugiura, M. (1964), Hourly values of the equatorial Dst for IGY, *Annals of the International Geophysical Year*, *35*(pp945-948), Pergamon Press.

Summers, D., R. M. Thorne, and F. Xiao (1998), Relativistic theory of wave-particle resonant diffusion with application to electron acceleration in the magnetosphere, *J. Geophys. Res.*, 103, A9, doi:10.1029/98JA01740.

Summers, D., B. Ni, and N. P. Meredith (2007), Timescales for radiation belt electron acceleration and loss due to resonant wave-particle interactions: 2. Evaluation for VLF chorus, ELF hiss, and electromagnetic ion cyclotron waves, *J. Geophys. Res.*, 113, A04219, doi:10.1029/2007JA012678.

Summers, D., B. Ni, N. P. Meredith, R. B. Horne, R. M. Thorne, M. B. Moldwin and R. R. Anderson (2008), Electron scattering by whistler-mode ELF hiss in plasmaspheric plumes, *J. Geophys. Res.*, 112, A04207, doi:10.1029/2006JA011993.

Thorne, R. M. (1977), Energetic radiation belt electron precipitation: a natural depletion mechanism for stratospheric ozone, *Science*, *195*(4275):287-9.

Thorne, R. M. (1980), The importance of energetic particle precipitation on the chemical composition of the middle atmosphere, *Pure and Appl. Geophys.*, *118*(1).

Thorne, R. M. (2010), Radiation belt dynamics: The importance of wave-particle interactions, *Geophys. Res. Lett.*, *37*(22), doi:10.1029/2010GL044990.

Thorne, R. M., W. Li, B. Ni, Q. Ma, J. Bortnik, D. N. Baker, H. E. Spence, G. D. Reeves, M. G. Henderson, C. A. Kletzing, W. S. Kurth, G. B. Hospodarsky, D. Turner and V. Angelopoulos (2013), Evolution and slow decay of an unusual narrow ring of relativistic electrons near L∼3.2 following the September 2012 magnetic storm, *Geophys. Res. Lett.*, *40*(14), doi:10.1002/grl.50627.

Thorne, R. M., W. Li, B. Ni, Q. Ma, J. Bortnik, D. N. Baker, H. E. Spence, G. D. Reeves, M. G. Henderson, C. A. Kletzing, W. S. Kurth, G. B. Hospodarsky, J. B. Blake, J. F. Fennell, S. G. Claudepierre and S. G. Kanekal (2013), Van Allen probe evidence of relativistic radiation belt electron acceleration by magnetospheric chorus, *Nature*, *504*, doi:10.1038/nature12889.

Turner, D. L., Y. Shprits, M. Hartinger, and V. Angelopoulos (2013), Explaining sudden losses of outer radiation belt electrons during geomagnetic storms, *Nature Phys.*, *8*, doi:10.1038/nphys2185.

Turunen, E., P. T. Verronen, A. Seppälä, C. J. Rodger, M. A. Clilverd, J. Tamminen, C. F. Enell, and T. Ulich (2009), Impact of different energies of precipitating particles on nox generation in the middle and upper atmosphere during geomagnetic storms, *J. Atmos. Sol. Terr. Phys.*, *71*, 1176–1189, doi:10.1029/2002GL016513.

Verronen, P. T., C. J. Rodger, M. A. Clilverd, and S. Wang (2011), First evidence of mesospheric hydroxyl response to electron precipitation from the radiation belts, *J. Geophys. Res.*, *116*(D07307), doi:10.1029/2010JD014965.

Verronen, P. T., M. Andersson, C. J. Rodger, M. A. Clilverd, S. Wang and E. Turunen (2013), omparison of modeled and observed effects of radiation belt electron precipitation on mesospheric hydroxyl and ozone, *J. Geophys. Res.*, *118*, doi:10.1002/jgrd.50845.

Simon Wedlund, M., M. A. Clilverd, C. J. Rodger, K. Cresswell-Moorcock, N. Cobbett, P. Breen, D. Danskin, E. Spanswick, and J. V. Rodriguez (2014), A statistical approach to determining energetic outer radiation belt electron precipitation fluxes, *J. Geophys. Res.*, *119*, doi:10.1002/2013JA019715

Whittaker, I. C., R. J. Gamble, C. J. Rodger, M. A. Clilverd and J.-A. Sauvaud (2013), Determining the spectra of radiation belt electron losses: Fitting DEMETER IDP observations for typical and storm-times, *J. Geophys. Res.*, doi:10.1002/2013JA019228

Whittaker, I. C., C. J. Rodger, M. A. Clilverd and J.-A. Sauvaud (2014), The effects and correction of the geometric factor for the POES/MEPED electron flux instrument using a multi-satellite comparison, *J. Geophys. Res.*, under review.

Yando, K., R. M. Millan, J. C. Green, and D. S. Evans (2011), A Monte Carlo simulation of the NOAA POES Medium Energy Proton and Electron Detector instrument, *J. Geophys. Res.*, *118*, doi:10.1002/jgra.50584

Figure 1: *A schematic of the of the wave activity in the radiation belts and plasmasphere adapted from Summers, Ni and Meredith [2007, Figure 21]. The angle from the vertical shows the magnetic local time while the radial distance gives the L shell value. The grey shaded area shows the morning MLT sector that we use in this study to determine the chorus affected zone outside the plasmapause, ranging from 01:00 to 08:00. The purple shaded area shows the afternoon MLT sector which we investigate to determine the plasmapspheric hiss induced fluxes inside the plasmapause, with an MLT range of 11:00 to 16:00.*

Figure 2: *a) The median Dst values associated with the 103 geomagnetic storms identified for our superposed epoch analysis, after SPE removal. b) The >300 keV morning MLT epoch plot using a* log_{10} *colour scale, showing peak precipitation from chorus (*t *= 0) and hiss (*t *= 3 to 7 days). The solid line represents the non-MLT dependent plasmapause location and the dashed line shows a +0.5* L *offset which separates the chorus and hiss induced precipitating flux. c) The >300 keV afternoon MLT epoch on the same scale and format as panel b). The dashed line represents a +0.75* L *offset from the O'Brien and Moldwin model.*

Figure 3: *The electron flux variation shown during our superposed epoch analysis for the morning MLT sector 01:00 to 08:00. All precipitating flux panels are shown with units of* $cm^{-2}sr^{-1}s^{-1}$. *The top left panel shows the median >30 keV electron flux, the top right panel shows the >100 keV electron flux and the lower left panel shows the >300 keV electron flux, all are shown on a* log_{10} *color scale. The lower right panel shows the spectral index from a power law fitting of the three energy ranges. The modeled plasmapause location from Figure 2 has been included on all panels as the dashed black line (O'Brien and Moldwin non MLT-dependent Dst model + 0.5* L*).*

Figure 4: *(Left) the >30 keV precipitating electron flux at different distances from the plasmapause* (L_{pp}) *are plotted, ranging from the plasmapause (top left panel) to 3* L *outside the plasmapause (lower left panel). The dark blue solid line shows the observed flux after superposed epoch analysis and the red dashed line shows the model flux from Equation* (3). *(Right) The spectral index from the power law fit of the three MEPED electron energy channels at the same distances from the plasmapause as the left panels. The blue solid line shows the spectral index observed and the red dashed line shows the simulation from Equation* (4).

Figure 5: *Simulations of the superposed epoch analysis using Equations* (3) *and* (4)*. The left panels show the >30 keV flux and the right panels show the spectral index. The top row contains the observed data, the middle row shows the simulation from Equation* (3) *and* (4) *respectively and the lower panels show the same simulation with a minimum flux (lower left, Equation* (5)*) and maximum spectral index (lower right) filter applied. The black dashed line shows the morning MLT plasmapause position.*

Figure 6: *The electron flux epochs for the afternoon MLT sector (11:00 to 16:00). The top left panel shows the median >30 keV electron flux, the top right panel shows the >100 keV electron flux and the lower left panel shows the >300 keV electron flux, all are shown on a* log_{10} *color scale. The lower right panel shows the P6 MEPED telescope superposed epoch analysis, this telescope includes relativistic electrons with energies >800 keV. The modeled afternoon MLT plasmapause location from Figure 2 has been included on all panels as the dashed black line (O'Brien and Moldwin non MLT-dependent Dst model + 0.75 L).*

Figure 7: **a) to d)** *The afternoon MLT sector (11:00-16:00) >300 keV electron flux observations at L shells of 3.3, 3.7, 4.1 and 4.5. The solid blue line shows the instrument flux and the red dashed line shows the simulation of the flux at each L shell as calculated by Equation* (6)*.* **e)** *The >300 keV storm epoch from the lower left panel of Figure 6 on a linear color scale emphasising the variation in flux inside the plasmapause by reducing the color range scale.* **f)** *The full simulation of the >300 keV flux inside the plasmapause created using Equation* (6)*, on the same color scale as panel e) and using a 84 hour mean Dst.* **g)** *shows the P6 observations from the lower right panel of Figure 6 on a linear color scale.* **h)** *The P6 simulation generated from Equation* (7)*, on the same linear color scale as panel g) working on a 96 hour mean Dst with a 1 day delay. The black dashed line in the epoch plots is the modeled plasmapause from Figure 2.*

Figure 8: *a) A DEMETER ICE superposed epoch analysis of lowerband chorus wave power around geomagnetic storms within the operating period of the satellite. The plasmapause model used for the POES data is also shown on this plot. b) A comparison*

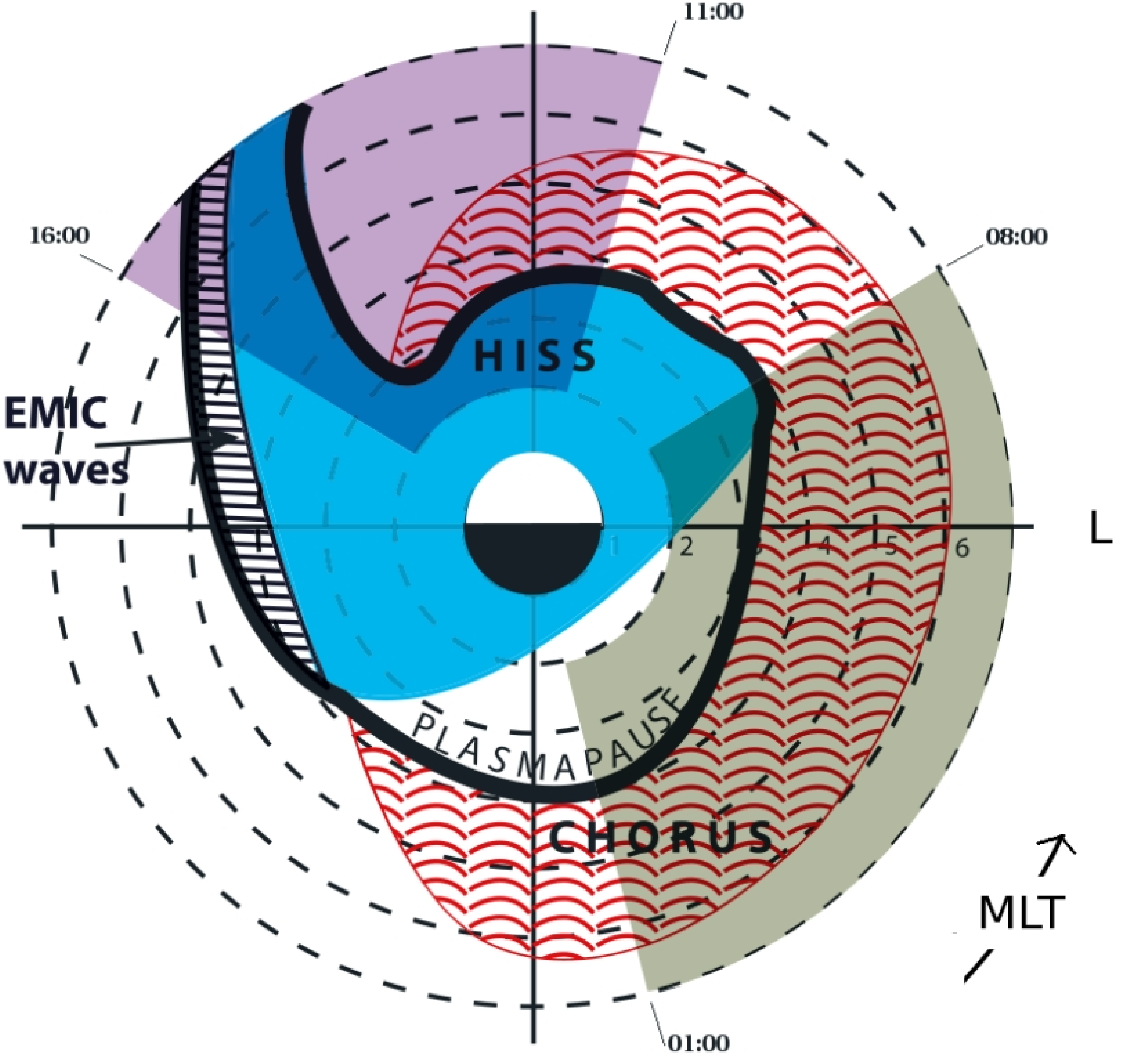
11:00
16:00
08:00
01:00
EMIC
waves
HISS
PLASMAPAUSE
CHORUS
L
1
2
3
4
5
6
MLT

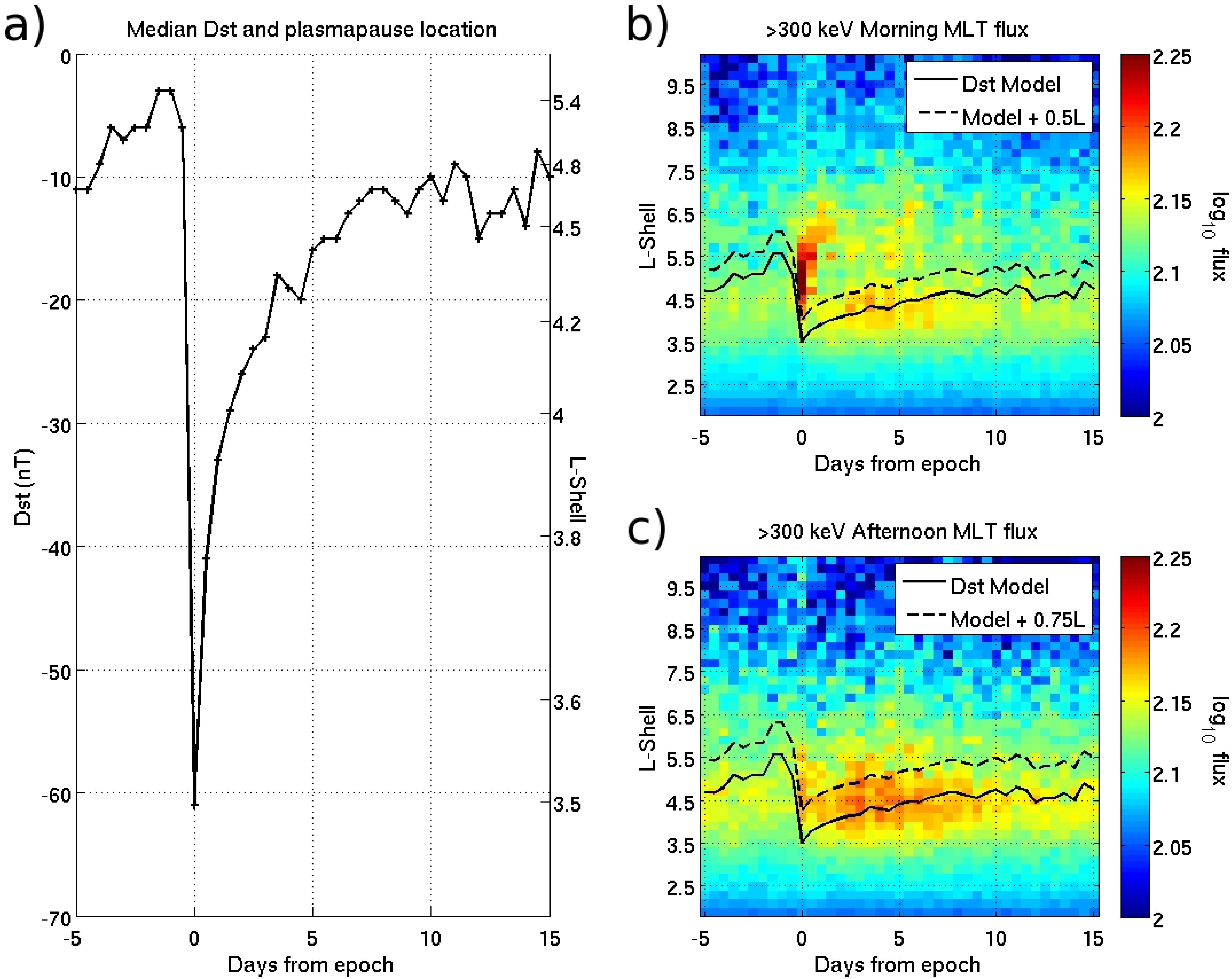

a)
Median Dst and plasmapause location
Dst (nT)
L-Shell
Days from epoch
0
-10
-20
-30
-40
-50
-60
-70
5.4
4.8
4.5
4.2
4
3.8
3.6
3.5
-5
0
5
10
15
b)
>300 keV Morning MLT flux
Dst Model
Model + 0.5L
L-Shell
Days from epoch
$\log_{10}$ flux
9.5
8.5
7.5
6.5
5.5
4.5
3.5
2.5
2.25
2.2
2.15
2.1
2.05
2
c)
>300 keV Afternoon MLT flux
Dst Model
Model + 0.75L
L-Shell
Days from epoch
$\log_{10}$ flux

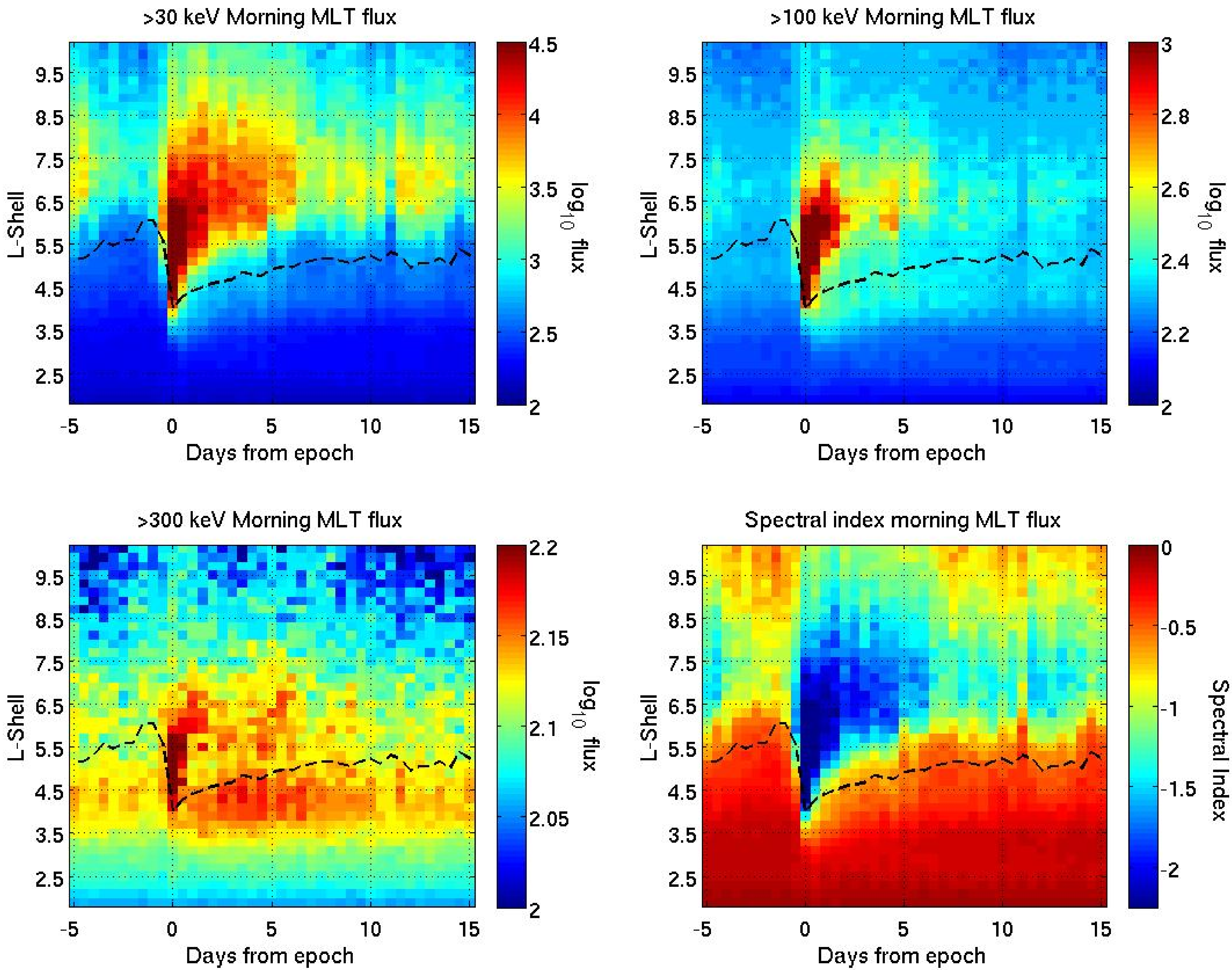
>30 keV Morning MLT flux
>100 keV Morning MLT flux
>300 keV Morning MLT flux
Spectral index morning MLT flux
L-Shell
Days from epoch
log10 flux
Spectral Index
9.5
8.5
7.5
6.5
5.5
4.5
3.5
2.5
-5
0
5
10
15
4.5
4
3.5
3
2.5
2
2.8
2.6
2.4
2.2
2.2
2.15
2.1
2.05
0
-0.5
-1
-1.5
-2

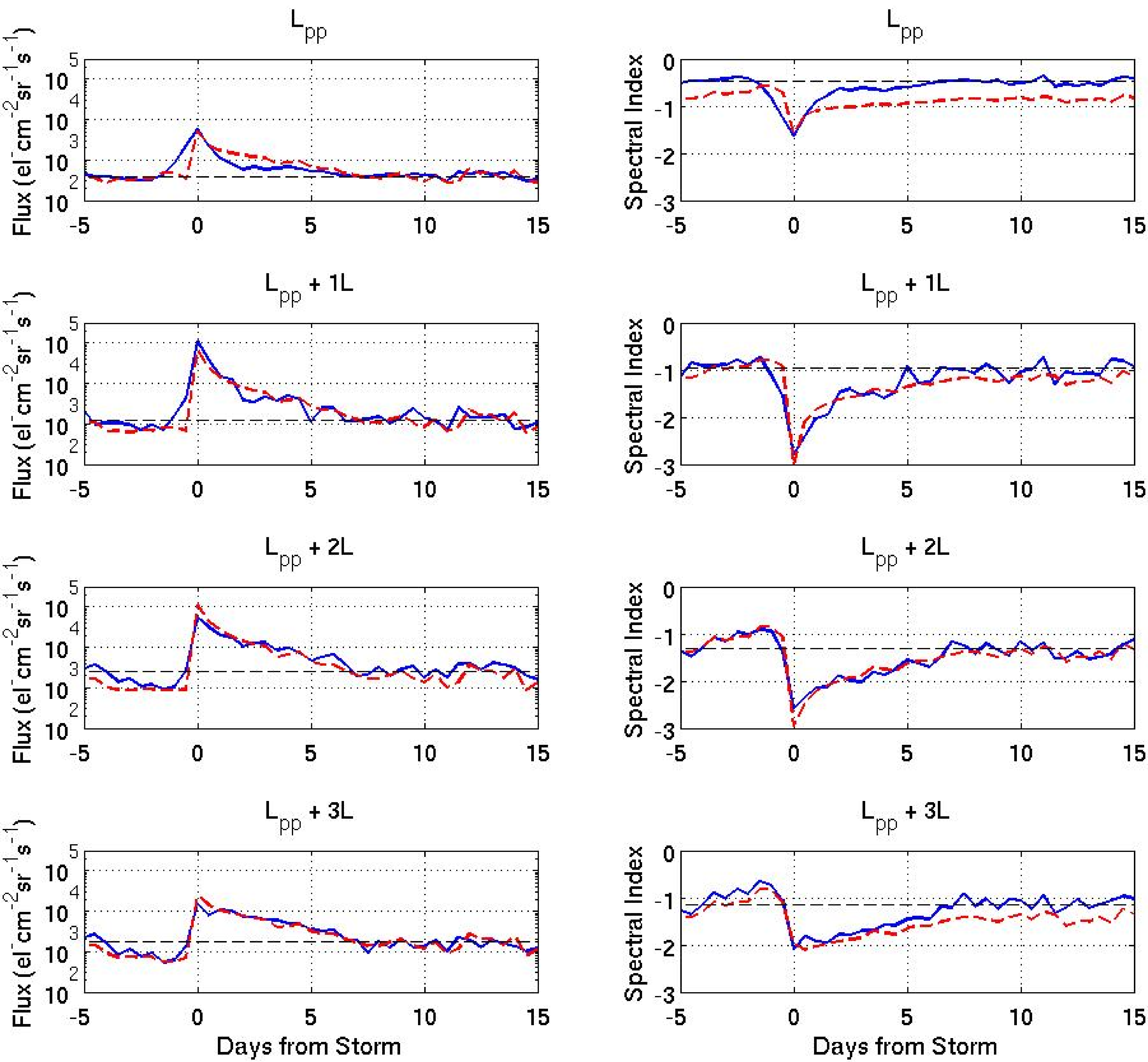

L_pp
L_pp + 1L
L_pp + 2L
L_pp + 3L
Flux (el cm^-2 sr^-1 s^-1)
Spectral Index
Days from Storm

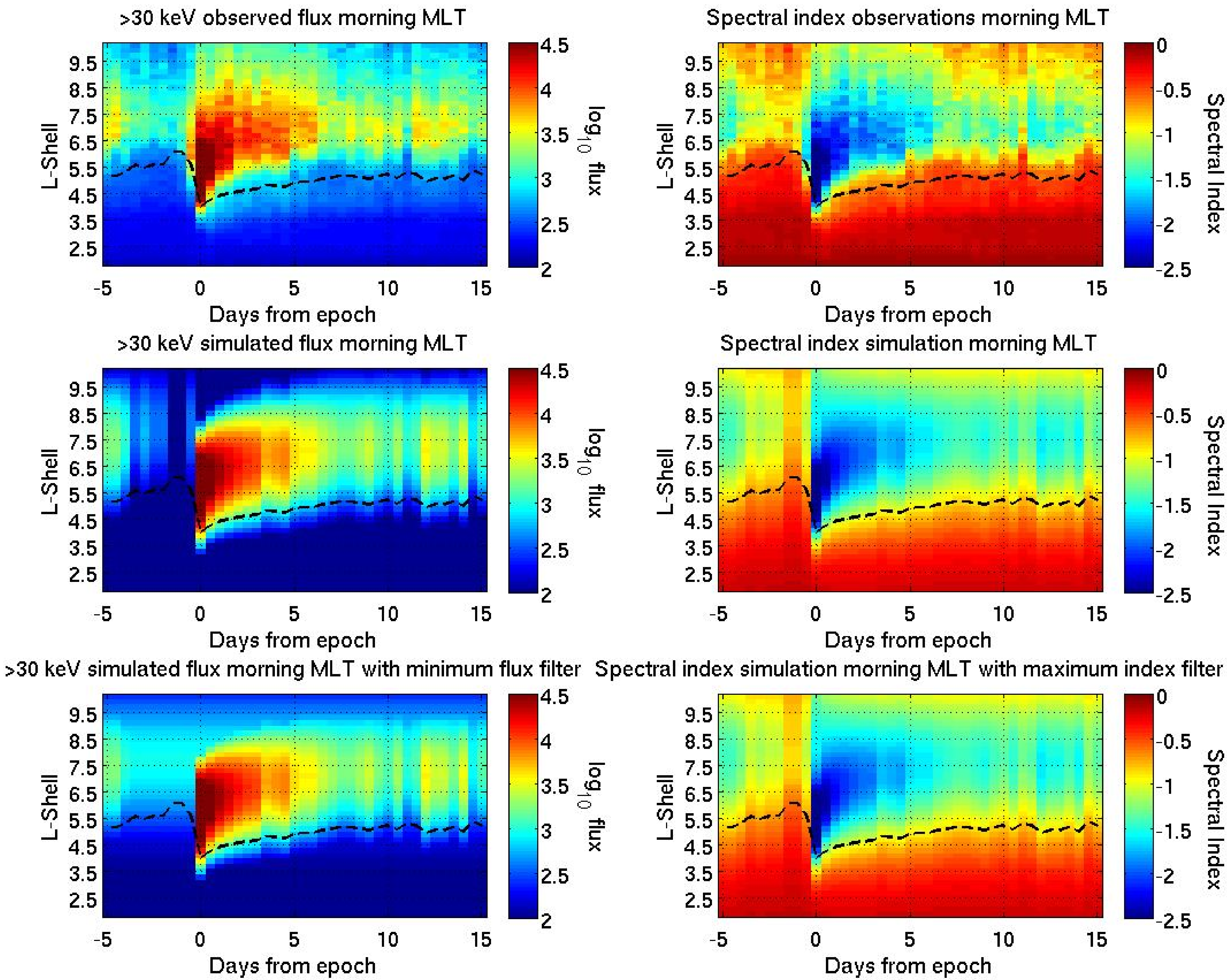
>30 keV observed flux morning MLT
Spectral index observations morning MLT
>30 keV simulated flux morning MLT
Spectral index simulation morning MLT
>30 keV simulated flux morning MLT with minimum flux filter
Spectral index simulation morning MLT with maximum index filter
L-Shell
Days from epoch
log10 flux
Spectral Index

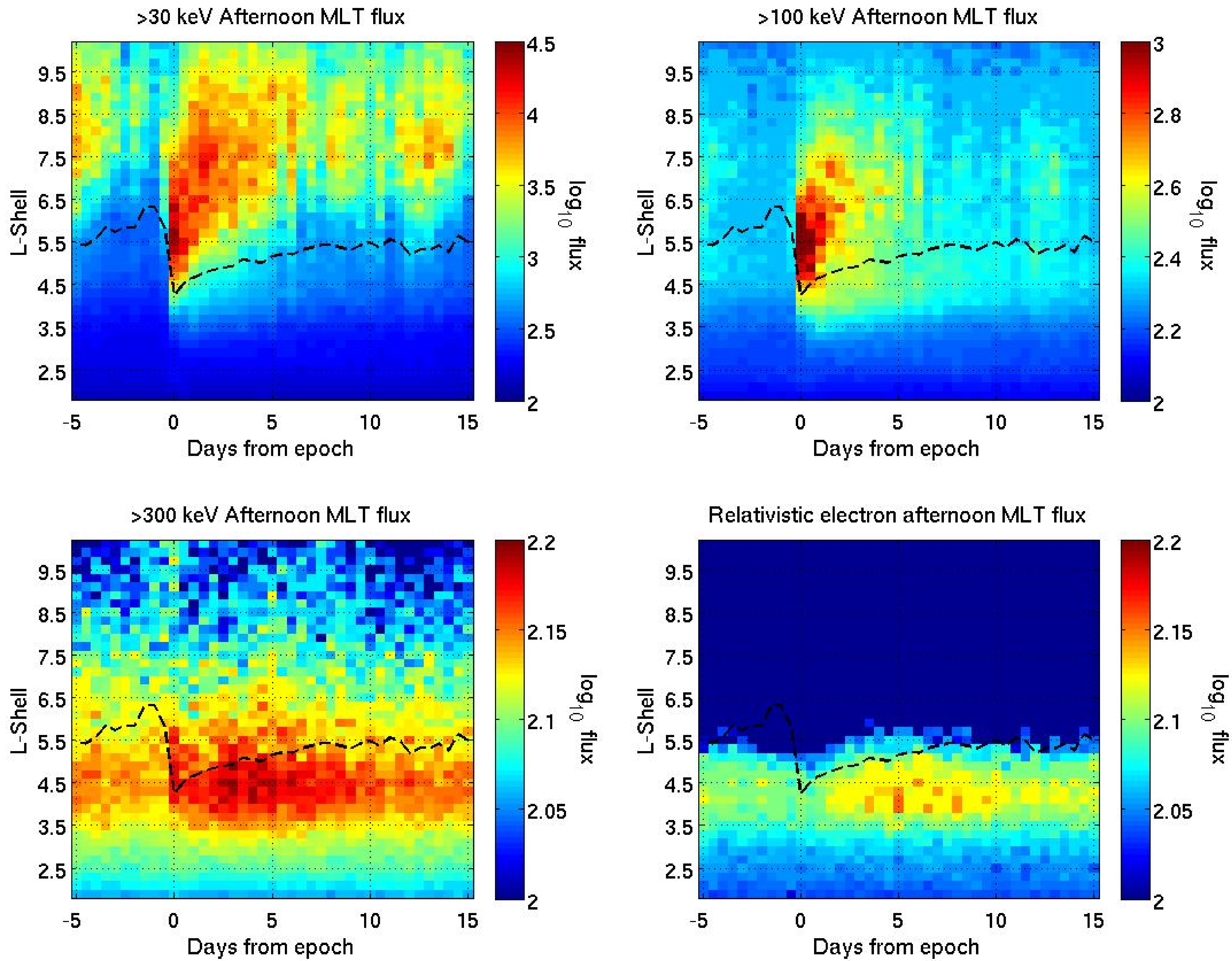

>30 keV Afternoon MLT flux
>100 keV Afternoon MLT flux
>300 keV Afternoon MLT flux
Relativistic electron afternoon MLT flux
L-Shell
Days from epoch
log10 flux

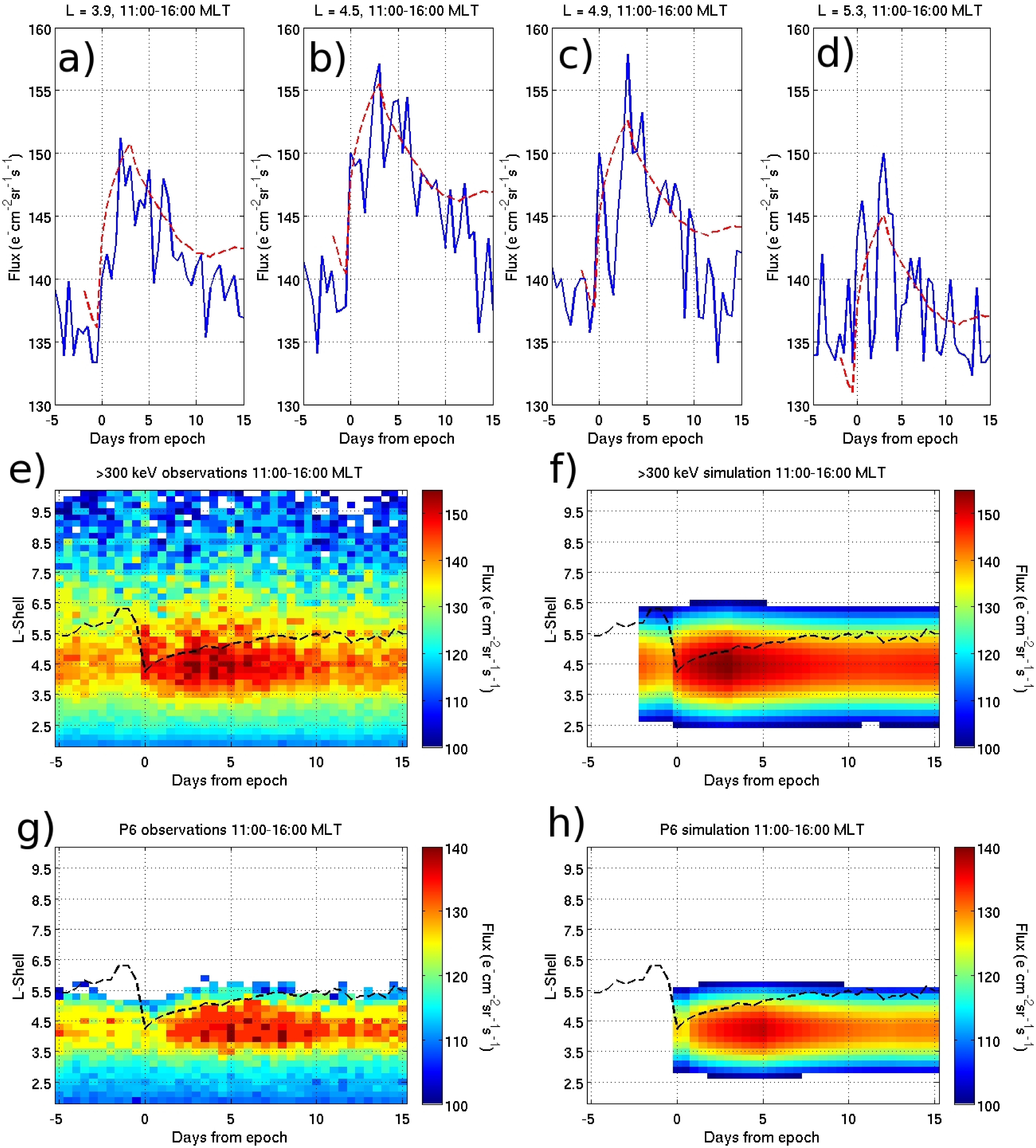

L = 3.9, 11:00-16:00 MLT
L = 4.5, 11:00-16:00 MLT
L = 4.9, 11:00-16:00 MLT
L = 5.3, 11:00-16:00 MLT
a)
b)
c)
d)
Flux (e cm^-2 sr^-1 s^-1)
Days from epoch
e)
>300 keV observations 11:00-16:00 MLT
f)
>300 keV simulation 11:00-16:00 MLT
g)
P6 observations 11:00-16:00 MLT
h)
P6 simulation 11:00-16:00 MLT
L-Shell

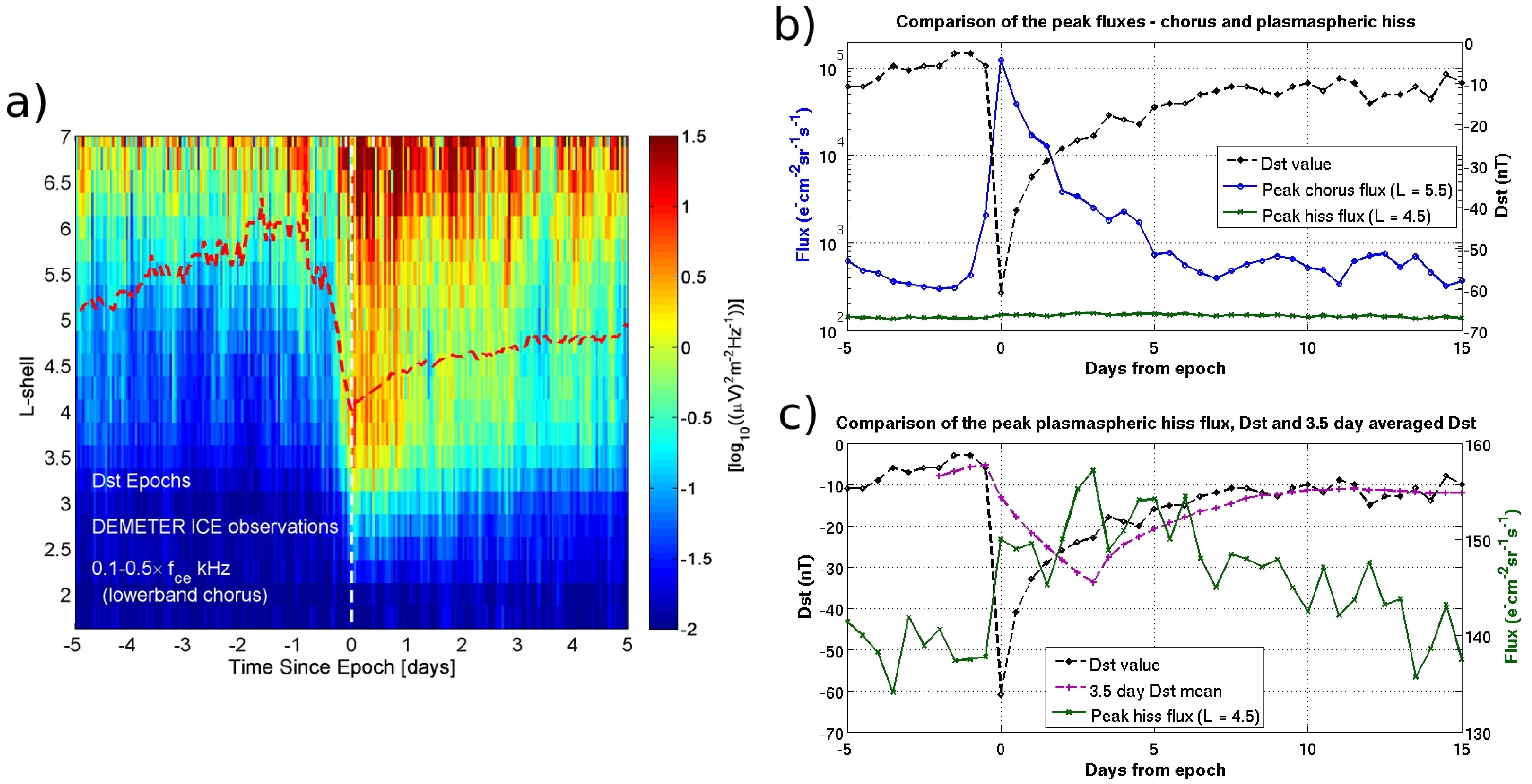

a)
Dst Epochs
DEMETER ICE observations
0.1-0.5× f ce kHz
(lowerband chorus)
L-shell
Time Since Epoch [days]
[log10((μV)2m-2Hz-1))]
b)
Comparison of the peak fluxes - chorus and plasmaspheric hiss
Dst value
Peak chorus flux (L = 5.5)
Peak hiss flux (L = 4.5)
Flux (e-cm-2sr-1s-1)
Dst (nT)
Days from epoch
c)
Comparison of the peak plasmaspheric hiss flux, Dst and 3.5 day averaged Dst
Dst value
3.5 day Dst mean
Peak hiss flux (L = 4.5)
Dst (nT)
Flux (e-cm-2sr-1s-1)
Days from epoch